Journal of Molecular Liquids xxx (xxxx) 118695

Contents lists available at ScienceDirect

Journal of Molecular Liquids

journal homepage: www.elsevier.com/locate/molliq

Multistep phase transition in 1-decyl-3-methylimidazolium nitrate ionic liquid

Hiroshi Abe, Hiroaki Kishimura

Department of Materials Science and Engineering, National Defense Academy, Yokosuka 239-8686, Japan

ARTICLE INFO

Article history:
Received 28 September 2021
Received in revised form 5 January 2022
Accepted 3 February 2022

Keywords:
Ionic liquids
Cooling rate effect
Quasiequilibrium
Long periodic layered structure
Small- and wide-angle X-ray scattering

ABSTRACT

Cooling-rate dependent multistep phase transition of 1-decyl-3-methylimidazolium nitrate ($[C_{10}mim][NO_3]$) was investigated at low temperature (LT) by conducting simultaneous small- and wide-angle X-ray scattering and differential scanning calorimetry (DSC) measurements. Above 9 °C/min (nonequilibrium), crystallization of $[C_{10}mim][NO_3]$ was suppressed upon cooling, whereas cold crystallization appeared upon heating. At the cooling rate region between 5 °C/min and 8 °C/min (quasiequlibrium), a multistep phase transition was identified on the DSC thermal traces. The Bragg reflection at the lowest scattering angle was located at a different position from that of the prepeak in the liquid state. A long periodic layered structure was formed at LT.

1. Introduction

Ionic liquids (ILs) emerged as novel solvents [1,2] with unique characteristics. For instance, ILs exhibit nanoheterogeneity even in the liquid state [3–11]. For 1-alkyl-3-methylimidazolium ($[C_nmim]^+$)-based ILs, where *n* indicates the alkyl chain length, nanoheterogeneity was theoretically demonstrated on the basis of molecular dynamics (MD) simulations [3–6]. In a simulation box, nanoheterogeneity can be easily tuned by the *n* value. Experimentally, a prepeak of $[C_nmim]^+$-based ILs was observed by small- and wide-angle X-ray scattering (SWAXS) [7–11]. Recently, the nanoheterogeneity of ILs is summarized in the literature [12–14]. In addition to the nanoheterogeneity of the $[C_nmim]^+$ cations, their molecular conformations contribute to the liquid or solid properties of ILs. The degrees of freedom of the conformations of the $[C_nmim]^+$ cations were estimated by density functional theory (DFT) calculations [15–19], indicating that their conformational stabilities extensively varied depending on *n*. The observed Raman bands were also assigned using DFT calculations [16,18,20].

Meanwhile, the anion component of ILs also plays an important role in its properties and is a key factor for the design of task-specific ILs [21]. For instance, calculation of the interaction energy of $[C_4mim][X]$ provided the anion ranking with basicity values [22], showing that the interaction energy decreases in the order of $F^- > Cl^- > Br^- > [NO_3]^- > I^- > SCN^-$. At low temperature (LT), the crystal structure of $[C_2mim][NO_3]$ is monoclinic ($P2_1/n$) [23], and a nonplanar conformer of $[C_2mim]^+$ existed in the unit cell. Phase transitions of $[C_2mim][NO_3]$ were examined at LT [24] and high pressure (HP) [25,26], and an HP-crystal polymorph and phase transitions with multiple pathways could be clearly distinguished using HP-SWAXS [26]. The presence or absence of an HP-inherent planar' conformer of $[C_2mim][NO_3]$ can alter the pathways of the phase transitions. In the case of $[C_4mim][NO_3]$, subsequent phase changes were detected upon heating via heat capacity measurements [27]. By conducting simultaneous wide-angle X-ray scattering and differential scanning calorimetry (DSC), two crystal phases were identified upon heating [28]. In contrast to $[C_nmim][NO_3]$ ($n = 2$ and 4), $[C_6mim][NO_3]$ and $[C_8mim][NO_3]$ did not crystallize either upon cooling or heating [29]. Furthermore, the effect of the long alkyl chain on the phase transitions of $[C_nmim][NO_3]$ was examined using MD simulations [30–32]. Several kinds of crystal structures of $[C_{14}mim][NO_3]$ were obtained in the simulation box [31]. Near the temperature of the phase transition from crystal to liquid crystal (LC), an intermediate molecular order as a metastable state was formed upon losing the polar bilayers.

Glass transition dynamics and crystallization kinetics of pyrrolidinium-based ILs were examined by changing the cooling rate [33]. The crystallization tendency of ILs was obtained by the crystallization rate.

Abbreviations: DFT, Density functional theory; DSC, Differential scanning calorimetry; HP, High pressure; IL, Ionic liquids; LC, Liquid crystal; LT, Low temperature; MD, Molecular dynamics; SWAXS, Small- and wide-angle X-ray scattering

E-mail address: ab@nda.ac.jp (H. Abe).

https://doi.org/10.1016/j.molliq.2022.118695
0167-7322/

Nonequilibrium behaviors of ILs were observed in the LT- and HP-phase transitions [34]. Crystal polymorphs and multiple pathways of the phase transitions are understood by introducing a crystal energy landscape [35], which is described by various energy minima of crystals reflecting conformational flexibility. Conversely, the crystal nucleation process of propylene carbonate was represented on a time – temperature transformation diagram [36], which indicated that the nucleation process was sensitive to the cooling rate. More interestingly, the heterogeneous dynamics of two-dimensional aggregates was demonstrated, considering the morphological hierarchy [37]. The formation of a nonequilibrium pattern was induced by a competition between pairwise short-range attraction and long-range repulsion.

In this study, we investigated the LT-phase behaviors of $[C_n\text{mim}][NO_3]$ (n = 2, 4, 6, 8, and 10) by changing the cooling rate. A multistep phase transition of 1-decyl-3-methylimidazolium nitrate ($[C_{10}\text{mim}][NO_3]$) was clarified via simultaneous SWAXS and DSC measurements. Moreover, we found that the LT crystal phase possessed a long periodic layered structure and that the lattice constant along the stacking direction was entirely different from the correlation length in the liquid state.

2. Experimental section

Commercially available $[C_2\text{mim}][NO_3]$ (assay > 98.0%) from Tokyo Chemical Industry Co., Ltd. and $[C_4\text{mim}][NO_3]$ from Sigma-Aldrich were used. $[C_6\text{mim}][NO_3]$, $[C_8\text{mim}][NO_3]$, and $[C_{10}\text{mim}][NO_3]$ (assay > 98.0%) were purchased from Angene Chemical. For all samples, vacuum drying was conducted for 48 h. Simultaneous SWAXS and DSC measurements were conducted using a vertical goniometer (SmartLab, Rigaku) [38] to clarify the complicated phase behaviors [39,40]. Cu Kα radiation (λ = 1.542 Å) was used for incident X-ray. The DSC windows used for SWAXS were metal-coated Mylar films. For the simultaneous measurements, a temperature range of – 100 °C to 50 °C was used, and the cooling and heating rates were 0.75 °C/min – 16 °C/min. During the simultaneous measurements, dry nitrogen gas was passed at 20 mL/min to reduce moisture. The scattering vector Q was defined as $4\pi(\sin\theta)/\lambda$ ($Å^{-1}$), where the scattered angle was 2θ.

The observed SWAXS patterns were analyzed using the *CONOGRAPH* software [41] and the *ab initio* structure determination program in *FOX* [42]. *CONOGRAPH* determined the crystal system and lattice parameters, and the molecular arrangements in the unit cell were simulated using *FOX*, which uses global optimization algorithms.

3. Results

3.1. Phase behaviors of $[C_n\text{mim}][NO_3]$ (n = 2, 4, 6, 8, and 10)

Fig. 1 displays the LT-phase transitions of $[C_n\text{mim}][NO_3]$ (n = 2, 4, 6, 8, and 10) at a cooling and heating rate of 5 °C/min. As can be observed in the figure, which also indicates the temperatures of crystallization, cold crystallization, melting, and glass transition (T_C, T_{CC}, T_m, and T_g, respectively), the phase transitions were influenced by the alkyl chain length, n. Generally, cold crystallization is defined by the stabilization process from the metastable phases to the stable crystal phases upon heating [43]. No prepeak was observed for $[C_2\text{mim}][NO_3]$ in the liquid state, suggesting that this IL did not exhibit nanoheterogeneity [29]. Thus, a charge network was preferred in $[C_2\text{mim}][NO_3]$. The molecular arrangement in the unit cell satisfied the charge network [23]. Upon cooling, $[C_2\text{mim}][NO_3]$ crystallized at – 10.7 °C (T_C) [26], and the crystal melted at 42.6 °C (T_m) upon heating. Meanwhile, the crystallization was completely suppressed in $[C_4\text{mim}][NO_3]$ upon cooling (5 °C/min) [28], indicating that the supercooled effect was enhanced in $[C_4\text{mim}][NO_3]$. Upon heating, cold crystallization occurred at –40.9 °C (T_{CC}), and the crystal structure

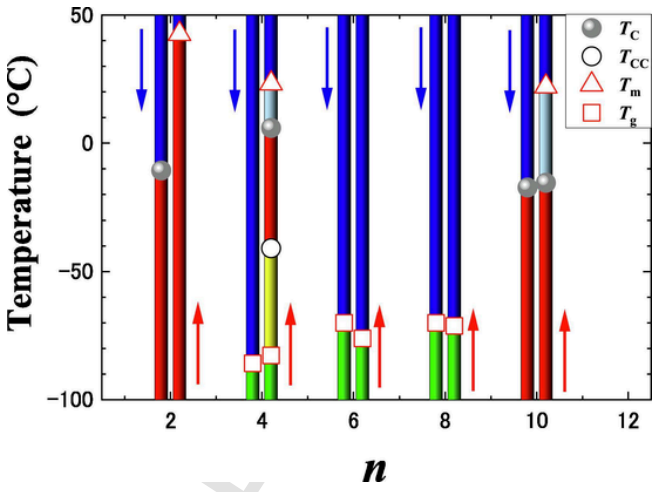

Fig. 1. Phase changes of $[C_n\text{mim}][NO_3]$ (n = 2, 4, 6, 8, and 10) at 5 °C/min. T_C, T_{CC}, T_m, and T_g represent the temperatures of crystallization, cold crystallization, melting, and glass transition, respectively. The blue and red arrows indicate the cooling and heating processes, respectively.

was found to be monoclinic. Further heating induced a solid–solid phase transition resulting in the formation of an orthorhombic lattice. Upon heating, the crystal polymorph of $[C_4\text{mim}][NO_3]$ reflected complicated molecular interactions. A small-angle neutron scattering analysis revealed a distinct prepeak in ILs with larger n, i.e., $[C_6\text{mim}][NO_3]$ and $[C_8\text{mim}][NO_3]$ [29]. The nanoheterogeneity was well developed in both ILs and could influence the crystal nucleation and growth at LT. In fact, neither crystallization nor cold crystallization occurred in $[C_6\text{mim}][NO_3]$ and $[C_8\text{mim}][NO_3]$ (Fig. 1). For $[C_{10}\text{mim}][NO_3]$, a long periodic layered structure was observed upon cooling. The phase transition behavior of $[C_{10}\text{mim}][NO_3]$ is described in Section 3.3.

The different phase transition behaviors of the $[C_n\text{mim}][NO_3]$ series can be explained in terms of the duality of their ionic and organic nature [44]. Thus, on the one hand, crystallization and cold crystallization were observed in $[C_2\text{mim}][NO_3]$ and $[C_4\text{mim}][NO_3]$, respectively, because of their ionic nature. On the other hand, an LC-like phase was observed in ILs with large n, namely, $[C_{10}\text{mim}][NO_3]$, as a result of its organic nature. In this case, the packing efficiency of the long alkyl chain of the $[C_{10}\text{mim}]^+$ cation was preferred over the charge network. Additionally, the alkyl chain length dependence of the density of $[C_n\text{mim}][NO_3]$ (n = 2, 4, 6, and 8) [29,30] supports the ionic and organic duality. High density is derived from Coulombic interactions, whereas low density is observed in ILs with long alkyl chains, because of their loosely packed nanoheterogeneity. The ionic nature (n = 2 and 4) and organic nature (n = 10) were clearly distinguished according to the LT phase behaviors, with the glass transition of $[C_6\text{mim}][NO_3]$ and $[C_8\text{mim}][NO_3]$ appearing as an intermediate state. Because of a competition between ionic and organic interactions, small crystal embryos could not exceed the critical size of crystal nucleation. The duality of the ionic and organic nature of $[C_n\text{mim}]NO_3]$ is illustrated by the phase behavior plot shown in Fig. 1.

3.2. Cooling rate effect of $[C_n\text{mim}][NO_3]$ (n = 2, 4, 6, and 8)

Recently, a significantly slow phase transition of $[C_8\text{mim}][BF_4]$ was reported [45]. Generally, the phase transitions of the ILs are sensitive to thermal treatments. The cooling rate effect of the phase transitions is caused by a nonequilibrium property as seen in glassy materials. Glass transition of ILs is influenced by the cooling rate, and dynamic fragility as a function of glass transition temperature is plotted to classify the anion effect [46]. Thus, the cooling rate dependence of the phase transitions of $[C_n\text{mim}][NO_3]$ (n = 2, 6, and 8) was examined by DSC (Fig.

2a). The phase transition of [C_2mim][NO_3] was simple both upon cooling and heating [26]. With increasing cooling rate, the crystallization temperature (T_C) of [C_2mim][NO_3] increased. However, at 16 °C/min, T_C decreased because of rapid cooling. Conversely, [C_6mim][NO_3] and [C_8mim][NO_3] showed a glass transition without crystallization at a cooling rate of 1 °C/min – 17 °C/min (Fig. 2a). Upon heating, cold crystallization was also suppressed in [C_6mim][NO_3] and [C_8mim][NO_3]. Significantly, glass was formed in [C_6mim][NO_3] and [C_8mim][NO_3] even by changing the cooling rate. In other [$C_n$mim][X] systems (X = BF_4 or PF_6), the glass transition of [C_6mim][X] and [C_8mim][X] occurred [47]. With increasing cooling rate, the glass transition temperature (T_g) of [C_6mim][NO_3] and [C_8mim][NO_3] slightly increased. This tendency was also seen in other ILs [46].

[C_4mim][NO_3] showed a complicated phase behavior on the cooling rate scale (Fig. 2b). At a cooling rate below 2.0 °C/min, the crystal polymorph of [C_4mim][NO_3] appeared upon cooling (Fig. S1). The multistep phase transition of [C_4mim][NO_3] was sensitive to the cooling rate and represented a nonequilibrium effect [34]. At a cooling rate above 3.0 °C/min, crystallization was not induced upon cooling (Fig. S1). Therefore, [C_4mim][NO_3] is regarded as an intermediated state between the crystal (n = 2) and glass (n = 6 and 8) states. In a crossover alkyl chain length (n = 4), the phase transition behaviors of [C_4mim][NO_3] were easily influenced by the cooling rate as a nonequilibrium factor. Not only upon cooling but also upon heating, the cooling rate effect was observed. The glass transition and cold crystallization of [C_4mim][NO_3] upon heating appeared at a heating rate above 1.0 °C/min (Fig. S1). In quaternary ammonium ILs [48], the thermogram upon heating indicated that the glass transition and cold crystallization occurred at – 75 °C (T_g) and – 45 °C (T_{CC}), respectively. In the case of [C_4mim][NO_3], at a cooling rate of 1.0C/min –2.0 °C/min, glass and crystal coexisted at the minimum temperature. Moreover, upon heating, two exothermal peaks were observed at a heating rate of 1.0C/min –2.0 °C/min. Here, it is emphasized that a glassy state was superimposed at a cooling rate of 1.0C/min –2.0 °C/min in addition to a crystal state.

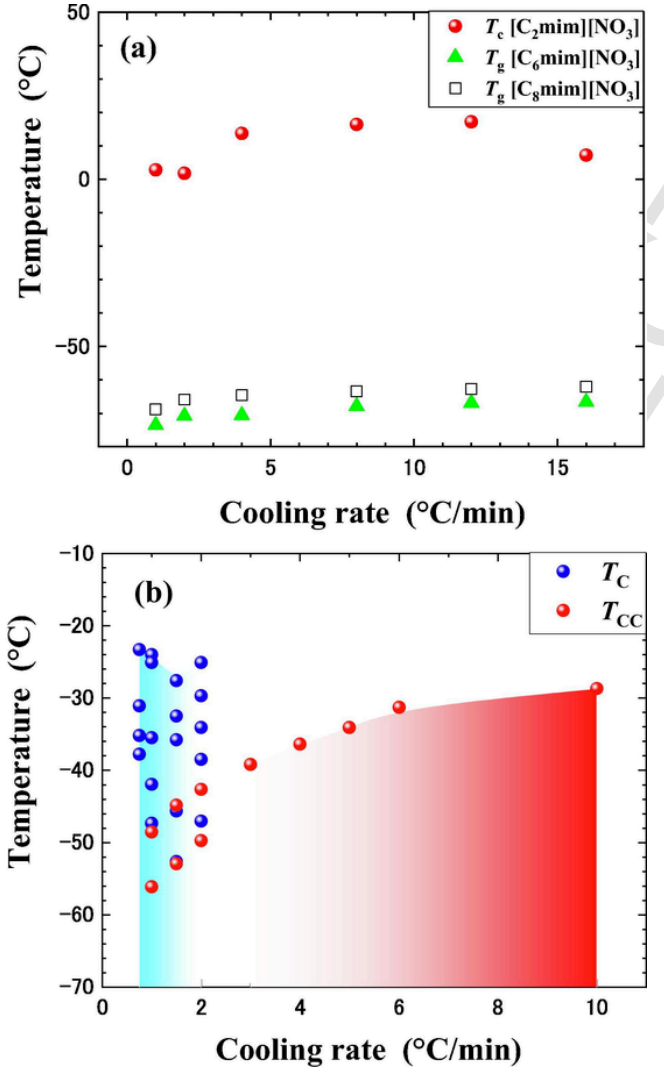

Fig. 2. (a) Cooling rate dependence of the crystallization temperature (T_C) of [C_2mim][NO_3] and glass transition temperature (T_g) of [$C_n$mim][NO_3] (n = 6 and 8). (b) Cooling rate dependence of crystallization upon cooling and cold crystallization upon heating of [C_4mim][NO_3].

3.3. Cooling rate effect of [C_{10}mim][NO_3]

Generally, as a nonequilibrium process, the formation of solid states depends on the cooling rate, and rapid cooling resulted in glass transition [49,50]. Fig. 3 shows the DSC thermal traces of [C_{10}mim][NO_3] at various cooling and heating rates. At a cooling rate of 14.3 °C/min, crystallization did not occur upon cooling. T_g was found to be –57.5 °C. Upon heating, the glass transition took place almost at the same T_g. With increasing temperature, cold crystallization was observed, which was accompanied by a sharp exothermal peak. Finally, the crystal melted, affording an endothermal peak. At a cooling rate of 9.0 °C/min, partial crystallization was detected by the appearance of small exothermal peaks with weak Bragg reflections at –16.6 °C, denoted by the blue open circles in Fig. S2. Since the Bragg reflections appeared in the halo pattern derived from the supercooled liquid or in an amorphous state (Fig. S2), the latter coexisted with a partially crystalline state. Upon heating at a heating rate of 9.0 °C/min, cold crystallization occurred above T_g. On the DSC thermal traces upon heating, the weak exothermal peak at –13.6 °C and the weak endothermal peak at 8.3 °C were observed (Fig. S2). Because of the rapid scan of the SWAXS patterns at 9.0 °C/min, we cannot detect the structural changes at all. Bragg intensities were insufficient to distinguish the phase transitions. We deduce that these small peaks on the DSC thermal trace are derived from the conformational changes on the lattice sites. If conformational changes occur without orientational and positional changes in the unit cell, the SWAXS pattern could change a little. Overall, T_g, T_{CC}, and T_m at a cooling rate of 9.0 °C/min were comparable with those observed at a cooling rate of 14.3 °C/min (Fig. 3).

Drastic phase changes were induced at a cooling rate below 8.1 °C/min for [C_{10}mim][NO_3]. Three broad exothermal peaks appeared upon cooling at a cooling rate of 8.1 °C/min (Fig. 3). Since the cooling rate was high, the phase changes were not distinguished on the SWAXS patterns during the three-step crystallization. The observed multistep phase transition can be qualitatively understood by nonequilibrium theories [51], although a quantitative theoretical description has not been provided. Compared with the small exothermal peak at a cooling rate of 9.0 °C/min, a distinct multistep crystallization occurred despite the small difference in the cooling rate. It should be noticed that the crossover cooling rate of the phase transition of [C_{10}mim][NO_3] was found to be 9.0 °C/min. The crossover cooling rate is an important glass-forming factor. Considering that no halo pattern was observed (Fig. S3), [C_{10}mim][NO_3] fully crystallized upon cooling at a cooling rate of 8.1 °C/min. This result was in accordance with the absence of T_g on the thermal trace. Moreover, upon heating, a solid–solid phase transition with a small endothermal peak occurred near T_m. When the cooling rate was reduced to 6.8 °C/min, the exothermal peak ratio drastically changed. The lowest exothermal peak decreased, and the phase behavior upon heating was almost equivalent to that at 8.1 °C/min. The decreasing tendency of the lowest exothermal peak was enhanced at 5.0 °C/min. The lowest exothermal peak was not observed on the DSC thermal trace (Fig. 3), indicating the occurrence of a two-step phase

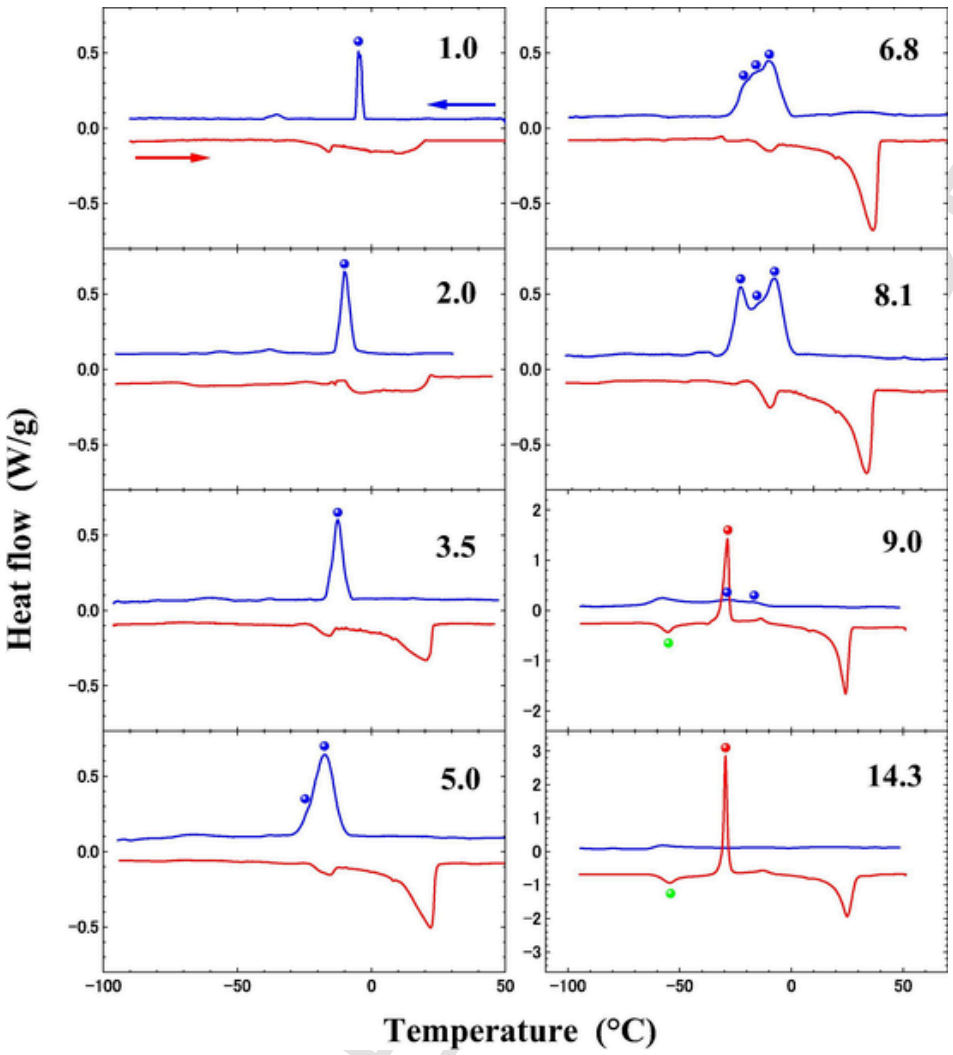

Fig. 3. Differential scanning calorimetry traces of $[C_{10}mim][NO_3]$ depending on the cooling rate. The numbers in the figure correspond to the cooling and heating rates. The multistep phase transitions upon cooling are indicated by the closed blue circles. Upon heating, the glass transition and cold crystallization are indicated by the green and red circles, respectively.

transition at 5.0 °C/min. Furthermore, at 3.5 °C/min, a single-phase transition occurred. Particularly below 5.0 °C/min, the T_C value increased, and the exothermal peak became sharper with a decrease in the cooling rate. Noteworthily, intrinsic multistep transitions were observed at intermediate cooling rates. Fig. 4 shows the cooling rate dependence of the transition temperatures. The cooling effect of the phase transition of $[C_{10}mim][NO_3]$ can be classified into three regions. Specifically, a nonequilibrium state was realized above 9 °C/min, because of the lack of crystallization (a fully frozen state) upon cooling. Conversely, a single-phase transition temperature occurred below 5 °C/min, which can be attributed to an equilibrium state. Between these cooling rate regions, the glass transition and cold crystallization upon heating were suppressed in $[C_{10}mim][NO_3]$ (Fig. 3). Compared with the crystal polymorph with glass forming of $[C_4mim][NO_3]$ at 1.0 °C/min −2.0 °C/min (Fig. S1), crystal polymorph without glass forming was observed in $[C_{10}mim][NO_3]$ at 5.0 °C/min – 8.1 °C/min. In $[C_{10}mim][NO_3]$ during the above cooling rate region, the coexistence of glass and crystal was not realized at the minimum temperature. The distinct boundaries on the cooling rate scale (Fig. 4) imply that the intermediate cooling region of 5.0 °C/min – 8.1 °C/min is a quasiequilibrium state. Recently, the concept of a quasiequilibrium state was introduced to describe the kinetic behavior of supercritical fluids [52]. The crystal polymorph without glass forming of $[C_{10}mim][NO_3]$ corresponds to quasiequilibrium, which does not belong to the equilibrium or nonequilibrium state.

3.4. Crystal structure of $[C_{10}mim][NO_3]$

Fig. 5 displays the representative simultaneous SWAXS and DSC measurements at 5.0 °C/min. At 23 °C, a prepeak distinctly appeared at 0.23 $Å^{-1}$ and a broad halo pattern centered at 1.5 $Å^{-1}$. When crystallization occurred at −17.3 °C (T_{C1}), sharp Bragg reflections (represented by the blue curve in Fig. 5) appeared on the SWAXS patterns, whereas the prepeak disappeared. The lowest Q position of the Bragg refraction was 0.145 $Å^{-1}$, which is not seen at the prepeak position. Generally, the LC phase of ILs is characterized by a sharp Bragg reflection at the prepeak position [53]. Therefore, the discrepancy between the positions of the prepeak and the lowest Q positioned Bragg reflection in the HP region for the crystal of $[C_{10}mim][Cl]$ is noteworthy [54]. The lowest peak of $[C_{10}mim][Cl]$ was identified as the 001 Bragg reflection. Moreover, the appearance of a series of 00ℓ Bragg reflections (ℓ = 1–5) was indicative of an HP-hybrid layered structure containing stacking and folding layers, where the stacking sequence is characterized by a long periodicity of 43 Å. At ambient pressure, the 00ℓ Bragg reflections (ℓ = 1, 2, 3, and 5) of $[C_{10}mim][NO_3]$ are represented by the closed blue circles in Fig. 5. Even at ambient pressure, a long periodic layered structure appeared

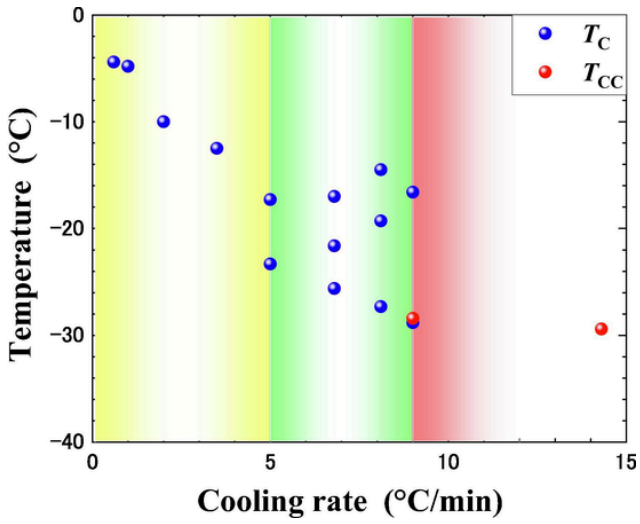

Fig. 4. Cooling rate dependence of the phase transitions. Crystallization upon cooling and cold crystallization upon heating are indicated by the blue and red circles, respectively. Above 9 °C/min, upon cooling, crystallization was suppressed.

in $[C_{10}mim][NO_3]$. Meanwhile, upon heating, a solid–solid phase transition was observed at −15.5 °C (T_{C2}) as a weak endothermal peak. This new phase is represented by green curves on the SWAXS patterns, where a new peak additionally appeared (denoted by the purple triangle in Fig. 5). The phase transition behavior of $[C_4mim][PF_6]$ upon heating [20] was characterized by solid–solid phase transitions that involved (i) conformational changes of $[C_4mim]^+$ and (ii) appearance of endothermal peaks. Hence, in the case of $[C_{10}mim][NO_3]$, a conformational change of $[C_{10}mim]^+$ could be induced upon heating. In fact, one of the new peaks at low Q position appeared between 001 and 002 Bragg reflections, and the new peak position coincided with that of the prepeak position (the purple closed triangle in Fig. 5). This suggests that a LC-like structure could be partially activated. Finally, the crystal melted at 22.1 °C (T_m), which was accompanied by the disappearance of the Bragg reflections.

Slow cooling experiments can probe the phase changes in detail. Fig. 6 reveals the simultaneous measurements of SWAXS and DSC at 1.0 °C/min. Even upon cooling, the LC phase appeared accompanying the crystal phase at T_{C1}. The sharp Bragg reflection appeared below T_{C1} (Fig. S4). Strong Bragg reflections of the crystal phase and a weak but sharp LC peak imply that the LC phase existed partially inside the crystal, permitting a lattice mismatch. With decreasing temperature, the LC phase vanished at T_{m1} with a small exothermal peak. Inversely, upon heating, the LC phase was observed with a weak endothermal peak. The LC phase of $[C_{10}mim][NO_3]$ is regarded as a stable phase. In the $[C_nmim][Cl]$ and $[C_nmim][PF_6]$ systems [53], the stable LC phase appeared above $n = 9$. Hence, the stable LC phase of $[C_{10}mim][NO_3]$ could be induced at $n = 10$.

To gain more insight into the HP-hybrid layered structure of $[C_{10}mim][Cl]$ [54], a crystal structure analysis was conducted. Fig. 7 displays the observed and calculated SWAXS patterns, and Table 1 lists the crystallographic data. The 00ℓ Bragg peaks indicated by the closed blue circles in Fig. 7 are sharp and large, which implies that the stacking layering was arranged favorably. Geometrically, the long lattice constant along the stacking direction (42.1 Å) hinders $[C_{10}mim]^+$ from adopting all-*trans* conformation, which contrasts with the LC phase (28.4 Å). In fact, the HP crystal of $[C_{10}mim][Cl]$, whose structure was determined using synchrotron radiation [54], contains the folded conformer of $[C_{10}mim]^+$. The determination of the detailed molecular arrangement of the $[C_{10}mim][NO_3]$ crystal was out of the scope of this study.

3.5. Model of the multistep phase transition processes

The multistep phase transition of $[C_{10}mim][NO_3]$ at LT provided a new insight for nonequilibrium science. To interpret the complicated behaviors observed, the following multistep factors must be considered: (i) long periodic layered structure, (ii) cooling rate dependence, (iii) rotational modes of the alkyl chain of $[C_{10}mim]^+$, (iv) nanoheterogeneity and density, and (v) duality of the ionic and organic nature. Fig. 8 illustrates one of the possible multiple phase transition processes as quasi-equilibrium states. The morphological images in Fig. 8 are based on a series of the MD simulations of $[C_nmim][NO_3]$ [30-32]. According to its large prepeak, the nanoheterogeneity of $[C_{10}mim][NO_3]$ developed well in the liquid state, where the correlation length was estimated to be 28.4 Å. With increasing alkyl chain length of $[C_nmim]^+$, the liquid

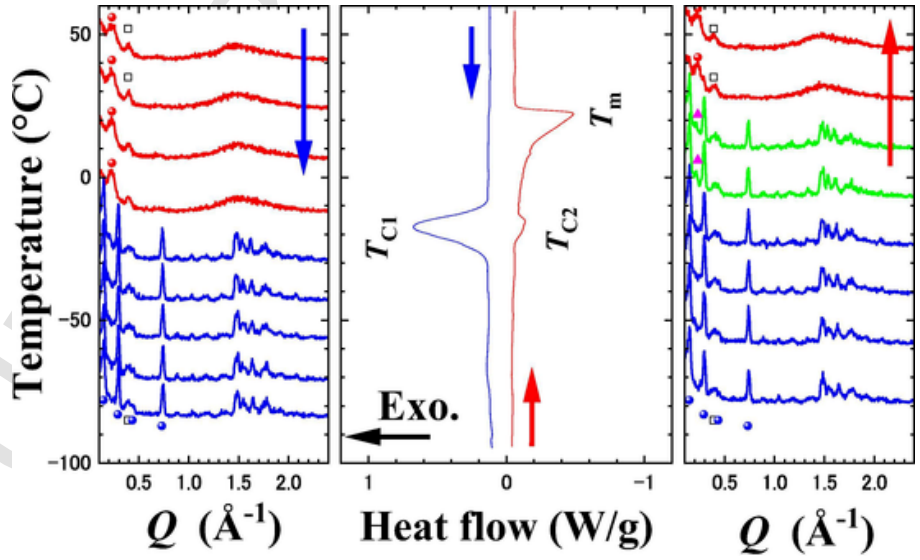

Fig. 5. Simultaneous small- and wide-angle X-ray scattering and DSC measurements at 5.0 °C/min. The open square represents scattering from an inner shroud of DSC. The closed red and blue circles indicate the prepeak and 00ℓ Bragg reflections, respectively. The closed purple triangle corresponds to additional Bragg reflection of a stable LC phase upon heating. The low Q position of the new Bragg reflection coincided with the prepeak position.

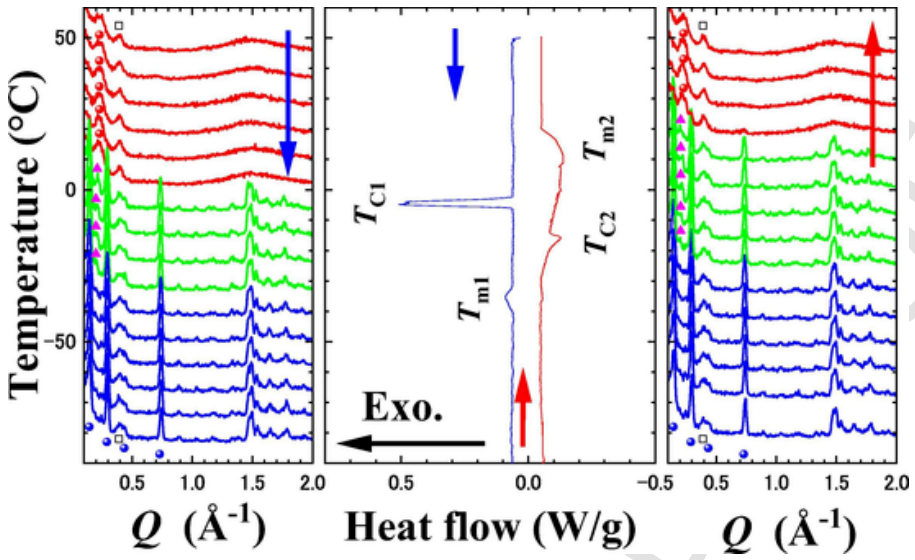

Fig. 6. Simultaneous measurements of SWAXS and DSC at 1.0 °C/min. The open square reveals scattering from an inner shroud of DSC. The closed red and blue circles indicate the prepeak and 00ℓ Bragg reflections, respectively. The closed purple triangle corresponds to an additional Bragg reflection of a stable LC phase.

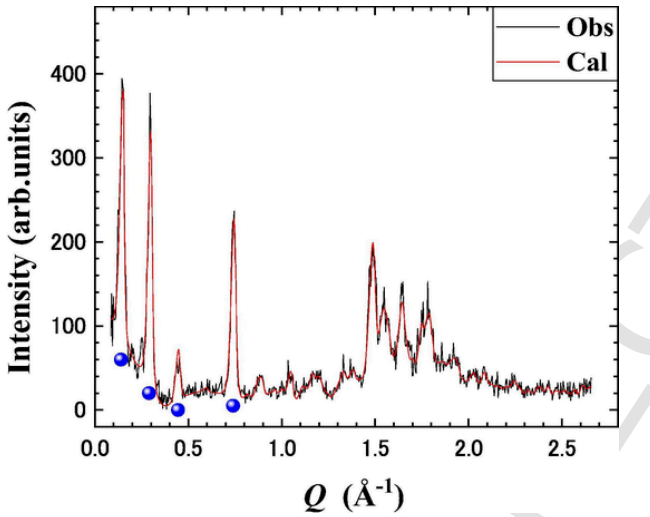

Fig. 7. Observed and calculated small- and wide-angle X-ray scattering patterns at − 95 °C. The cooling rate was 5.0 °C/min. The closed blue circles indicate the 00ℓ Bragg reflections.

Table 1
Crystallographic data of $[C_{10}mim][NO_3]$.

	a (Å)	*b* (Å)	*c* (Å)	α (°)	β (°)	γ (°)	*Z*	ρ (g/cm^3)	R_w (%)	*R* (%)
$P2_1/c$	15.426	42.065	6.660	90	99.12	90	12	1.33	18.1	13.2

density decreased [29], and the nanoheterogeneity developed further. Thus, in $[C_{10}mim][NO_3]$, the density fluctuation between relatively low- and high-density nanoregions is thermally activated. In the high-density nanoregion, the alkyl chains are well packed, whereas a cavity or folding of the $[C_{10}mim]^+$ cation is present in the low-density nanoregion. Moreover, in the simulation box of $[C_{12}mim][NO_3]$ [32], nonpolar nanodomains (cationic tail groups) indicated that parallel order of cationic side chains appears over the short range, with losing the orientational order between each nanodomains. It can be concluded that the cooling rate-dependent dynamics of the alkyl chain determines the phase transition processes. At high cooling rates (9 °C/min < d*T*/d*t*), the rotational motions of the alkyl chains are randomly frozen, thereby preventing crystal nucleation as a nonequilibrium effect. Below 9 °C/min, the thermally excited rotational modes are gradually suppressed. The collective motions of the alkyl chains are promoted, and crystal nucleation and growth locally and individually occur. Thus, in the early stage of crystal nucleation and growth, nanocrystal domains are randomly distributed with an orientation disorder. Here, the lattice constant along the stacking direction was 42.1 Å (Table 1).

Considering the intermediate interaction energy of $[NO_3]^-$ [22], it can be assumed that the ionic nature of $[C_{10}mim][NO_3]$ is not dominant. Since the nanoheterogeneous alkyl chain packing and motions as the organic component are effective, crystal growth on the nanoscale cannot continuously occur. At this stage (the first exothermal peak), small crystal domains were independently formed, and an arrangement of the nanocrystal domains is required for further cooling. Next, the origin of the second exothermal peak is discussed. In the second process of the phase transition, the orientational correlation among the nanocrystal domains in the medium range is indispensable to reach a long-range order. The orientational order of the nanocrystal domains induces the development of crystal domains on the mesoscopic scale. Finally, the third exothermal peak corresponds to the appearance of a homogeneous layered structure in the long range. At intermediate cooling rates (5.0–8.0 °C/min), a quasiequilibrium state can be realized, and the growth process cannot continuously occur upon cooling. This might be due to the occurrence of a partial pinning effect induced by nanoheterogeneity and weak ionic interaction between cations and anions. Consequently, the LT phase transition of $[C_{10}mim][NO_3]$ can be categorized into the above three processes.

4. Conclusions

The phase transition of $[C_{10}mim][NO_3]$ was examined using simultaneous SWAXS and DSC measurements. The phase transition was found to be quite sensitive to the cooling rate. At 5.0 °C/min – 8.0 °C/min (quasiequilibrium), three subsequent exothermal peaks were detected on the DSC thermal traces. Hidden information about the multistep phase transition could be extracted by analyzing the phase behaviors at the intermediate cooling rate. On the basis of the correlation length determined from the prepeak observed in the liquid state, an all-*trans* conformation can be deduced for $[C_{10}mim]^+$. The LT crystal structure of $[C_{10}mim][NO_3]$ was characterized by a long periodic layered structure, whose lattice constant was longer than that of the LC phase. Upon heating, an additional Bragg re-

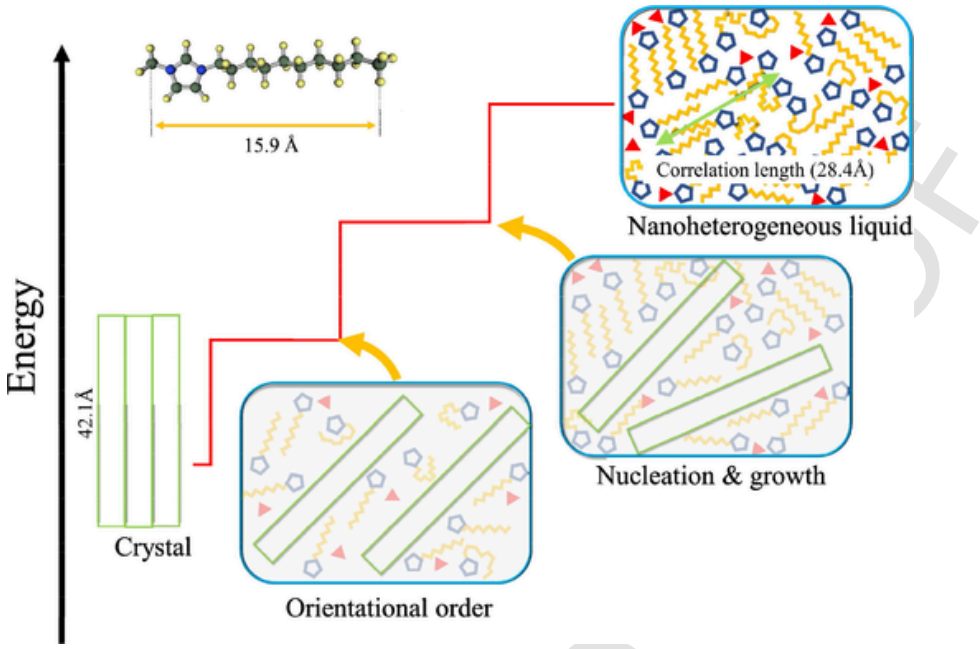

Fig. 8. Multistep phase transition processes upon cooling. The red closed triangles reveal the $[NO_3]^-$ anions.

flection was located at the prepeak position, which indicates that the LC crystal was a stable phase. Overall, the equilibrium, quasiequilibrium, and nonequilibrium phase behaviors of $[C_{10}mim][NO_3]$ could be clearly distinguished by changing the cooling rates.

CRediT authorship contribution statement

Hiroshi Abe: Conceptualization, Writing – original draft, Writing – review & editing. **Hiroaki Kishimura:** Data curation, Formal analysis.

Declaration of Competing Interest

The authors declare that they have no known competing financial interests or personal relationships that could have appeared to influence the work reported in this paper.

Acknowledgments

We thank Dr. F. Nemoto, Dr. T. Takekiyo and Professor Y. Yoshimura of the National Defense Academy for the helpful discussions.

Appendix A. Supplementary material

Supplementary data to this article can be found online at https://doi.org/10.1016/j.molliq.2022.118695.

References

[1] T. Welton, Ionic liquids: a brief history, Biophys. Rev. 10 (2018) 691–706.
[2] Z. Lei, B. Chen, Y.-M. Koo, D.R. MacFarlane, Introduction: Ionic Liquids, Chem. Rev. 117 (2017) 6633–6635.
[3] Y. Wang, G.A. Voth, Tail Aggregation and Domain Diffusion in Ionic Liquids, J. Phys. Chem. B 110 (37) (2006) 18601–18608.
[4] J.N.A. Canongia Lopes, A.A.H. Pádua, Nanostructural Organization in Ionic Liquids, J. Phys. Chem. B 110 (7) (2006) 3330–3335.
[5] A.A. Freitas, K. Shimizu, J.N. Canongia Lopes, Complex Structure of Ionic Liquids. Molecular Dynamics Studies with Different Cation–Anion Combinations, J. Chem. Eng. Data 59 (2014) 3120–3129.
[6] C.E.S. Bernardes, K. Shimizu, A.I.M.C. Lobo Ferreira, L.M.N.B.F. Santos, J.N. Canongia Lopes, Structure and Aggregation in the 1,3-Dialkyl-imidazolium Bis (trifluoromethylsulfonyl)imide Ionic Liquid Family: 2. From Single to Double Long Alkyl Side Chains, J. Phys. Chem. B 118 (2014) 6885–6895.
[7] A. Triolo, O. Russina, H.-J. Bleif, E. Di Cola, Nanoscale Segregation in room temperature ionic liquids, J. Phys. Chem. B 111 (18) (2007) 4641–4644.
[8] O. Russina1, A. Triolo, L. Gontrani, R. Caminiti, D. Xiao, L.G. Hines Jr, R.A. Bartsch, E.L. Quitevis, N. Plechkova, K.R. Seddon, Morphology and intermolecular dynamics of 1-alkyl-3-methylimidazolium bis{(trifluoromethane)sulfonyl}amide ionic liquids: structural and dynamic evidence of nanoscale segregation, J. Phys.: Condens. Matter 21 (2009) 424121–424129.
[9] W. Zheng, A. Mohammed, L.G. Hines, D. Xiao, O.J. Martinez, R.A. Bartsch, S.L. Simon, O. Russina, A. Triolo, E.L. Quitevis, Effect of Cation Symmetry on the Morphology and Physicochemical Properties of Imidazolium Ionic Liquids, J. Phys. Chem. B 115 (20) (2011) 6572–6584.
[10] O. Russina, A. Triolo, New experimental evidence supporting the mesoscopic segregation model in room temperature ionic liquids, Faraday Discuss. 154 (2012) 97–109.
[11] O. Russina, A. Triolo, L. Gontrani, R. Caminiti, Mesoscopic Structural Heterogeneities in Room-Temperature Ionic Liquids, J. Phys. Chem. Lett. 3 (2012) 27–33.
[12] R. Hayes, G.G. Warr, R. Atkin, Structure and Nanostructure in Ionic Liquids, Chem. Rev. 115 (2015) 6357–6426.
[13] K. Dong, X. Liu, H. Dong, X. Zhang, S. Zhang, Multiscale Studies on Ionic Liquids, Chem. Rev. 117 (2017) 6636–6695.
[14] Y.-L. Wang, B. Li, S. Sarman, F. Mocci, Z.-Y. Lu, J. Yuan, A. Laaksonen, M.D. Fayer, Microstructural and Dynamical Heterogeneities in Ionic Liquids, Chem. Rev. 120 (2020) 5798–5877.
[15] J.N. Canongia Lopes, J. Deschamps, A.A.H. Pádua, Modeling Ionic Liquids Using a Systematic All-Atom Force Field, J. Phys. Chem. B 108 (6) (2004) 2038–2047.
[16] Y. Umebayashi, T. Fujimori, T. Sukizaki, M. Asada, K. Fujii, R. Kanzaki, S. Ishiguro, Evidence of Conformational Equilibrium of 1-Ethyl-3-methylimidazolium in Its Ionic Liquid Salts: Raman Spectroscopic Study and Quantum Chemical Calculations, J. Phys. Chem. A 109 (2005) 8976–8982.
[17] S. Tsuzuki, A.A. Arai, K. Nishikawa, Conformational Analysis of 1-Butyl-3-methylimidazolium by CCSD(T) Level Ab Initio Calculations: Effects of Neighboring Anions, J. Phys. Chem. B 112 (26) (2008) 7739–7747.
[18] J. Kiefer, C.C. Pye, Structure of the Room-Temperature Ionic Liquid 1-Hexyl-3-methylimidazolium Hydrogen Sulfate: Conformational Isomerism, J. Phys. Chem. A 114 (24) (2010) 6713–6720.
[19] T. Endo, T. Higuchi, Y. Kimura, DFT Study on Conformation of 1-Alkyl-3-methylimidazolium with Ethyl, Propyl, Butyl, Pentyl, and Hexyl Group, Bull. Chem. Soc. Jpn. 93 (6) (2020) 720–729.
[20] T. Endo, T. Kato, K. Tozaki, K. Nishikawa, Phase Behaviors of Room Temperature Ionic Liquid Linked with Cation Conformational Changes: 1-Butyl-3-methylimidazolium Hexafluorophosphate, J. Phys. Chem. B 114 (2010) 407–411.
[21] K. Ueno, H. Tokuda, M. Watanabe, Ionicity in ionic liquids: correlation with ionic structure and physicochemical properties, Phys. Chem. Chem. Phys. 12 (2010) 1649–1658.
[22] P. Naert, K. Rabaey, C.V. Stevens, Ionic liquid ion exchange: exclusion from strong interactions condemns cations to the most weakly interacting anions and dictates reaction, equilibrium, Green Chem. 20 (2018) 4277–4286.
[23] J.S. Wilkes, M.J. Zaworotko, Air and Water Stable I-Ethyl-3-methylimidazolium Based Ionic Liquids, J. Chem. Soc., Chem. Commun. (1992) 965–967.
[24] V. Štejfa, J. Rohlíc˘ek, C. C˘. ervinka, Phase behaviour and heat capacities of selected 1-ethyl-3-methylimidazolium-based ionic liquids, J. Chem. Thermodyn. 142 (2020) 106020–106110.

[25] Y. Yoshimura, T. Takekiyo, H. Abe, N. Hamaya, High-pressure phase behavior of the room temperature ionic liquid 1-ethyl-3-methylimidazolium nitrate, J. Mol. Liq. 206 (2015) 89–94.
[26] H. Abe, T. Takekiyo, Y. Yoshimura, N. Hamaya, S. Ozawa, Crystal Polymorphs and Multiple Crystallization Pathways of Highly Pressurized 1-Ethyl-3-Methylimidazolium Nitrate, Aust. J. Chem. 72 (2) (2019) 87, https://doi.org/10.1071/CH18368.
[27] A.A. Strechan, A.G. Kabo, Y.U. Paulechka, A.V. Blokhin, G.J. Kabo, A.S. Shaplov, E.I. Lozinskaya, Thermochemical properties of 1-butyl-3-methylimidazolium nitrate, Thermochim. Acta 474 (1–2) (2008) 25–31.
[28] H. Abe, T. Takekiyo, Y. Yoshimura, K. Saihara, A. Shimizu, Anomalous Freezing of Nano-Confined Water in Room-Temperature Ionic Liquid 1-Butyl-3-Methylimidazolium Nitrate, ChemPhysChem 17 (8) (2016) 1136–1142.
[29] H. Abe, F. Nemoto, K. Hiroi, K. Ohishi, S. Takata, Spontaneous formations of nanoconfined water in ionic liquids by small angle neutron scattering, J. Mol. Liq., *in press*.
[30] W. Cao, Y. Wang, G. Saielli, Metastable State during Melting and Solid-Solid Phase Transition of $[C_n$Mim$][NO_3]$ (n = 4–12) Ionic Liquids by Molecular Dynamics Simulation, J. Phys. Chem. B 122 (1) (2018) 229–239.
[31] W. Cao, Y. Wang, Phase Behaviors of Ionic Liquids Heating from Different Crystal Polymorphs toward the Same Smectic-A Ionic Liquid Crystal by Molecular Dynamics Simulation, Crystals 9 (2019) 26–114.
[32] S. Li, Y. Wang, Percolation Phase Transition from Ionic Liquids to Ionic Liquid Crystals, Sci. Rep. 9 (2019) 13169–13178.
[33] W. Tu, G. Szklarz, K. Adrjanowicz, K. Grzybowska, J. Knapik-Kowalczuk, M. Paluch, Effect of Cation n-Alkyl Side-Chain Length, Temperature, and Pressure on the Glass-Transition Dynamics and Crystallization Tendency of the $[C_nC_1$Pyrr$]^+[Tf_2N]^-$ Ionic Liquid Family, J. Phys. Chem. C 123 (2019) 12623–12637.
[34] H. Abe, H. Kishimura, T. Takekiyo, Y. Yoshimura, N. Hamaya, Non-equilibriumprotic and aprotic ionic liquids: Measuring the distance from the equilibrium state, J. Mol. Liq. 283 (2019) 196–207.
[35] S.L. Price, From crystal structure prediction to polymorph prediction: interpreting the crystal energy landscape, Phys. Chem. Chem. Phys. 10 (15) (2008) 1996, https://doi.org/10.1039/b719351c.
[36] G. Szklarz, K. Adrjanowicz, M. Paluch, Cooling-Rate versus Compression-Rate Dependence of the Crystallization in the Glass-Forming Liquid, Propylene Carbonate, Cryst. Growth Des. 18 (2018) 2538–2544.
[37] T. Das, T. Lookman, M.M. Bandi, Morphology dictated heterogeneous dynamics in two-dimensional aggregatesSoft Matt. 12 (2016) 9674–9682.
[38] T. Arii, A. Kishi, Y. Kobayashi, A new simultaneous apparatus for X-ray diffractometry and differential scanning calorimetry (XRD-DSC), Thermochim. Acta 325 (2) (1999) 151–156.
[39] H. Abe, Y. Yoshimura, Y. Imai, T. Goto, H. Matsumoto, Phase behavior of room temperature ionic liquid – H_2O mixtures: *N*, *N*-diethyl-*N*-methyl-*N*-2-methoxyethyl ammonium tetrafluoroborate, J. Mol. Liq. 150 (2009) 16–21.
[40] H. Abe, H. Kishimura, M. Aono, Anomalous phase behavior of excess iodide in room-temperature ionic liquid: 1-methyl-3-propylimidazolium iodide, Chem. Phys. 502 (2018) 72–76.
[41] R. Oishi-Tomiyasu, Robust powder auto-indexing using many peaks, J. Appl. Cryst. 47 (2) (2014) 593–598.
[42] V. Favre-Nicolin, R. Cerny, *FOX*, 'free objects for crystallography': a modular approach to *ab initio* structure determination from powder diffraction, J. Appl. Cryst. 35 (2002) 734–743.
[43] Ł. Kolek, M. Massalska-Arodź, K. Adrjanowicz, T. Rozwadowski, K. Dychtoń, M. Drajewicz, P. Kula, Molecular dynamics and cold crystallization process in a liquid-crystalline substance with para-, ferro- and antiferro-electric phases as studied by dielectric spectroscopy and scanning calorimetry, J. Mol. Liq. 297 (2020) 111913–111918.
[44] R. Shi, Y. Wang, Dual Ionic and Organic Nature of Ionic Liquids, Sci. Rep. 6 (2016) 19644–19712.
[45] K. Watanabe, T. Komai, Very Slow Phase Transition from the Liquid to Mesophase and Phase-Coexistence in the Ionic Liquid $[C_8$mim$]BF_4$, Bull. Chem. Soc. Jpn. 94 (2) (2021) 508–512.
[46] R. Tao, E. Gurung, M.M. Cetin, M.F. Mayer, E.L. Quitevis, S.L. Simon, Fragility of ionic liquids measured by Flash differential scanning calorimetry, Thermochim. Acta 654 (2017) 121–129.
[47] J.D. Holbrey, K.R. Seddon, Ionic Liquids, Clean Products Proc. 1 (1999) 223–236.
[48] J.N. Curry, S.K. Shaw, Thermotropic Phase Transitions in Butyltrimethylammonium Bis(trifluoromethylsulfonyl)imide Ionic Liquids are Dependent on Heat Flux, J. Phys. Chem. B 123 (2019) 4757–4765.
[49] A. Gradys, P. Sajkiewicz, A.A. Minakov, S. Adamovsky, C. Schick, T. Hashimoto, K. Saijo, Crystallization of polypropylene at various cooling rates, Mater. Sci. Eng. A 413–414 (2005) 442–446.
[50] T. Lv, J. Li, S. Huang, H. Wen, H. Li, J. Chen, S. Jiang, Dynamics affected memory for crystallization behaviors of poly(D-lactic acid), Polymer 211 (2020) 123078–123079.
[51] J.F. Lutsko, How crystals form: A theory of nucleation pathways, Sci. Adv. 5 (2019) 7399–7408.
[52] S. Lee, J. Lee, Y. Kim, S. Jeong, D.E. Kim, G. Yun, Quasi-equilibrium phase coexistence in single component supercritical fluids, Nat. Commun. 12 (2021) 4630–4637.
[53] F. Nemoto, M. Kofu, O. Yamamuro, Thermal and Structural Studies of Imidazolium-Based Ionic Liquids with and without Liquid-Crystalline Phases: The Origin of Nanostructure, J. Phys. Chem. B 119 (2015) 5028–5034.
[54] H. Abe, N. Hamaya, Y. Koyama, H. Kishimura, T. Takekiyo, Y. Yoshimura, D. Wakabayashi, N. Funamori, K. Matsuishi, Long Periodic Structure of a Room-Temperature Ionic Liquid by High-Pressure Small-Angle X-Ray Scattering and Wide-Angle X-Ray Scattering: 1-Decyl-3-Methylimidazolium Chloride, ChemPhysChem 19 (2018) 1441–1447.